

CCAD: Compressed Global Feature Conditioned Anomaly Detection

Xiao Jin^{1,*}, Liang Diao^{2,*}, Qixin Xiao³, Yifan Hu³

Ziqi Zhang^{4,6}, Yuchen Liu⁵, Haisong Gu^{6,†}

¹Columbia University

²Ping An Property & Casualty Insurance Company

³University of Michigan

⁴University of California at Berkeley

⁵Stevens Institute of Technology

⁶VisionX LLC.

xj2285@columbia.edu, {diaoliang91, cml.bkl789, liuyuchen1119}@gmail.com,
 {qxiaocs, yfh}@umich.edu, haisonggu@ieee.org

Abstract

Anomaly detection holds considerable industrial significance, especially in scenarios with limited anomalous data. Currently, reconstruction-based and unsupervised representation-based approaches are the primary focus. However, unsupervised representation-based methods struggle to extract robust features under domain shift, whereas reconstruction-based methods often suffer from low training efficiency and performance degradation due to insufficient constraints. To address these challenges, we propose a novel method named Compressed Global Feature Conditioned Anomaly Detection (CCAD). CCAD synergizes the strengths of both paradigms by adapting global features as a new modality condition for the reconstruction model. Furthermore, we design an adaptive compression mechanism to enhance both generalization and training efficiency. Extensive experiments demonstrate that CCAD consistently outperforms state-of-the-art methods in terms of AUC while achieving faster convergence. In addition, we contribute a reorganized and re-annotated version of the DAGM 2007 dataset with new annotations to further validate our method’s effectiveness. The code for reproducing main results is available at <https://github.com/chloeqxq/CCAD>.

1 Introduction

Anomaly Detection (AD) is a crucial task in computer vision, particularly in industrial applications such as autonomous driving, medicine, and manufacturing, where it is essential to identify anomalous images and localize regions of anomalies. Unlike traditional supervised learning, AD faces the significant challenge of inaccessible anomalies during the training phase. Consequently, many existing AD methods adopt a zero-shot learning framework, where models are trained solely on nominal data, learning their distribution to

effectively discriminate anomalous instances based on noticeable deviations during the inference process [Bergman *et al.*, 2020; Defard *et al.*, 2021; Roth *et al.*, 2022].

Mainstream AD methods can be mainly categorized into three approaches: unsupervised-representation-based, reconstruction-based, and knowledge distillation-based methods. For unsupervised-representation-based methods, a feature extractor is trained to model normal data distribution, and some unsupervised learning approach (*e.g.*, k-nearest neighbors) is applied to detect anomalies. Recent works [Bergman *et al.*, 2020; Roth *et al.*, 2022; Hyun *et al.*, 2024] use models pretrained on large-scale datasets to extract the global feature space from the normal dataset, ensuring method generalization and pushing the accuracy limits of feature-based approaches. However, the domain gap between large-scale pre-training datasets and downstream data, along with the inflexibility of rule-based global feature selection, limits the performance of feature-based approaches. Knowledge distillation is another widely used AD approach. Knowledge of normal samples is transferred from a large pre-trained teacher model to small-scale student models. However, student models often exhibit inferior performance on anomaly samples compared to the teacher model. This disparity serves as a key indicator for detecting anomalies.

In reconstruction-based methods, image generation models trained solely on normal samples are employed to reconstruct anomalous samples into normal ones during the inference phase [Akçay *et al.*, 2019; Wyatt *et al.*, 2022; Zhang *et al.*, 2023a; Mousakhan *et al.*, 2023; He *et al.*, 2024]. By comparing the original sample with the reconstructed ones, anomaly locations can be identified.

As diffusion models progress in Generative AI, an increasing number of AD methods are now leveraging diffusion models as the core component for reconstruction-based approaches. As illustrated in Figure 1, [Wyatt *et al.*, 2022] (Figure 1a) is the pioneer in utilizing a diffusion model (DM) for anomaly detection. Subsequently, [Mousakhan *et al.*, 2023; He *et al.*, 2024] (Figure 1b) advances the reconstruction quality by conditioning it on the input images (local feature).

* indicates equal contribution.

† corresponding author: Haisong Gu (email: haisonggu@ieee.org).

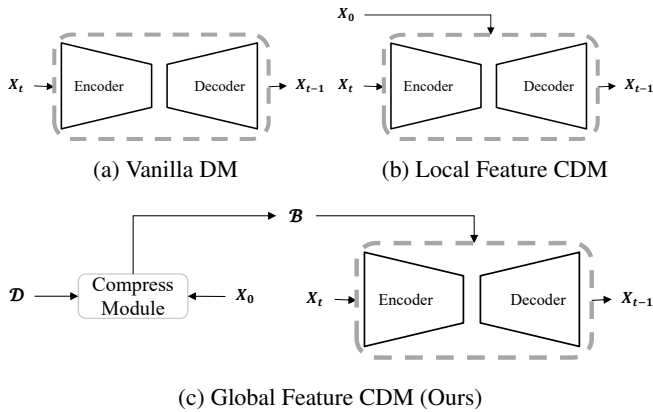


Figure 1: An overview of Diffusion Modules (DM) and Conditioned Diffusion Modules (CDM): (a) The vanilla DM operates without any condition. (b) A single sample x_0 is used as the condition (c) Compressed vectors \mathcal{B} representing the distribution of a whole dataset are served as the condition.

Nonetheless, the information provided by local features is inherently limited, and the absence of adequate prior conditions impairs training efficiency and constrains the potential for achieving higher accuracy. To address these challenges and improve both accuracy and resource efficiency in model training, we introduce a novel method: the Compressed Global Feature Conditioned Anomaly Detection Module (CCAD). This method integrates feature-based and reconstruction-based approaches, utilizing global features as auxiliary conditions to enhance reconstruction quality. Furthermore, CCAD incorporates a two-stage feature compression mechanism to optimize the trade-off between performance and efficiency (Figure 1c).

Here are the main contributions of our paper:

- We propose a method called CCAD that uses global features as prior conditions for reconstruction-based anomaly detection. To the best of our knowledge, this is the first time global features have been used to enhance the reconstruction quality of diffusion models.
- We explore the selection of global features and validate the feasibility and necessity of feature compression. We also propose a two-stage global feature compression mechanism that uses a coarse-to-fine approach to convert global features into prior conditions. This mechanism ensures both the performance and efficiency of CCAD.
- Extensive experiments verify the effectiveness of CCAD, supported by empirical analyses that illustrate how the proposed methods enhance anomaly detection performance. In addition, the DAGM 2007 dataset is revisited, and the images are re-annotated. Compared to the original ground truth, these new annotations are more accurate, providing a more reliable evaluation of anomaly detection methods. The annotated data is made publicly available.

2 Related Works

Mainstream anomaly detection (AD) methods can be categorized into three primary approaches: knowledge distillation-based, unsupervised-representation-based, and reconstruction-based methods.

2.1 Knowledge distillation-based approach

Knowledge distillation-based methods were used to transfer knowledge from a large, well-trained teacher model to a smaller student model, aiming to replicate the teacher's performance. S-T AD introduced a student-teacher framework using discriminative latent embeddings [Bergmann *et al.*, 2020], and EfficientAD [Batzner *et al.*, 2024] optimized the distillation process resulted in better efficiency and lower computational requires.

2.2 Unsupervised-representation-based approach

Earlier work [Yi and Yoon, 2020] depended on specific unsupervised training methods to achieve effective results on downstream datasets, as early pre-trained models struggled with generalization. However, advancements in pre-trained models have enabled recent approaches to extract anomalous image features and apply unsupervised techniques, such as KNN, to detect anomalies from globally extracted features. DN2 [Bergman *et al.*, 2020] utilized simple ResNets [He *et al.*, 2016] with high-level feature representations from pre-trained ImageNet. SPADE [Cohen and Hoshen, 2020] introduced the concept named as memory banks for better reuses of pre-trained features for both pixel-level and image-level anomaly detection. PaDiM [Defard *et al.*, 2021] later proposed the patch-level feature banks to estimate the patch-level Mahalanobis distances. PatchCore [Roth *et al.*, 2022] and Re-ConPatch [Hyun *et al.*, 2024] used similar patch-level memory banks, but they used coresets sampling methods to reduce the inference costs notably while retaining the higher performance.

These unsupervised learning methods heavily rely on the quality of global feature spaces from the pre-trained networks. Furthermore, previous methods are only limited on single-class AD tasks.

2.3 Reconstruction-based approach

This approach utilized generative models to reconstruct normal images. GANomaly [Akcay *et al.*, 2019] was the first work to apply GAN in reconstruction-based anomaly detection tasks. As diffusion models emerged as powerful generative tools, they were also adapted for reconstruction-based anomaly detection. Diffusion models was first proposed by DDPM [Ho *et al.*, 2020] in which gradually adding noise to data in a forward process and then learning to reverse this process in a way that can generate new data samples from pure noise. DDIM [Song *et al.*, 2020] improved DDPM by introducing a deterministic sampling process that reduced steps for faster, more efficient image generation. Later, Latent Diffusion Models (LDM) [Rombach *et al.*, 2022] optimized this process by working in a lower-dimensional latent space. ControlNet [Zhang *et al.*, 2023b] further enhanced diffusion models by adding spatial conditioning controls while preserving the original model's parameters.

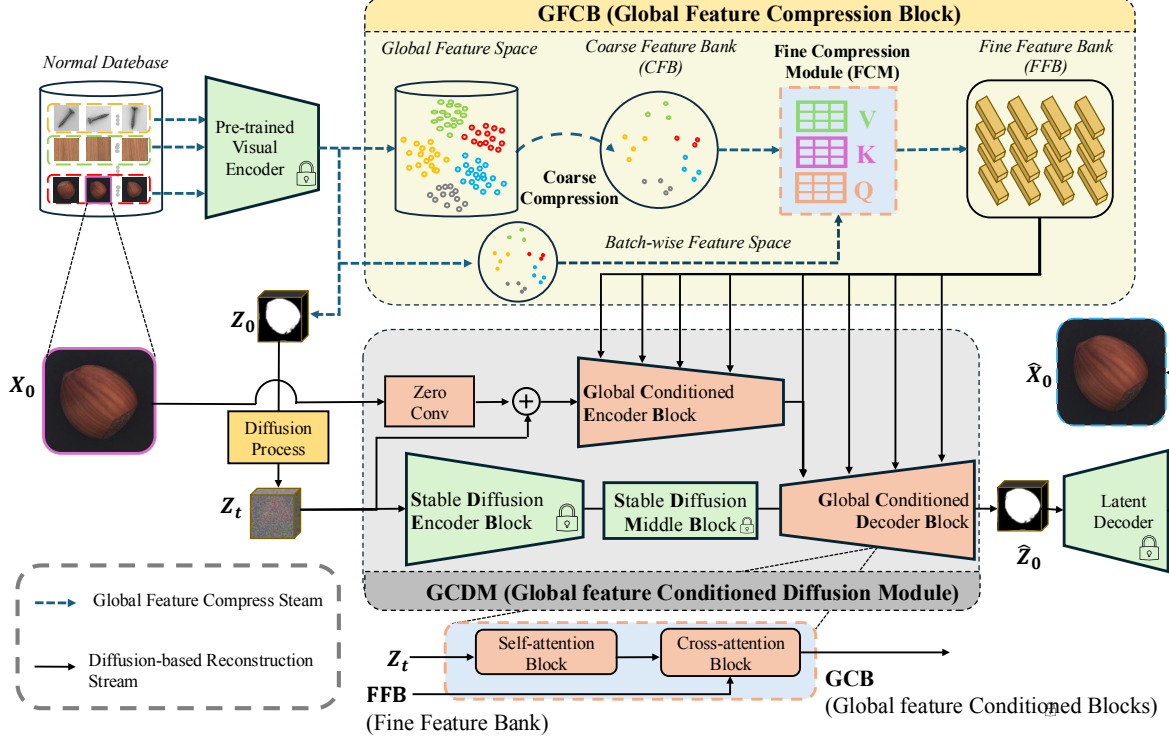


Figure 2: The framework of CCAD(F). Our method consists of two main part: Global Feature Compression Block (GFCB) and Global feature Conditioned Diffusion Module (GCDM). FFB denotes Fine Feature Bank, and GCB denotes Global Feature Conditioned Block.

Partial diffusion with simplex noise in DDPMs was employed by AnoDDPM [Wyatt *et al.*, 2022] to detect large abnormalities. DiffusionAD [Zhang *et al.*, 2023a] introduced a diffusion model with norm-guided and one-step denoising paradigm. Following this, DDAD [Mousakhan *et al.*, 2023] utilized a conditioned denoising diffusion model which enhanced the accuracy by reconstructing normal samples to match a target image. DiAD [He *et al.*, 2024] proposed a multi-class anomaly detection framework, combined with a pixel-space autoencoder, Semantic-Guided Network, and Spatial-aware Feature Fusion block, while POUTA [Wang *et al.*, 2024] leveraged encoder-decoder feature discrepancies.

3 Method

In this section, we introduce some necessary preliminaries and implementation of our CCAD method. As shown in Figure 2, our method consists of two streams: the Global Feature Compression Stream, which compresses the global feature space to obtain the global feature bank, and the Diffusion-based Reconstruction Stream, which uses the global feature bank as a condition to generate normal images. To meet different application requirements, we also design three variants: CCAD(F), CCAD(C), CCAD(V).

3.1 Preliminaries

Latent diffusion Module

The diffusion model is the foundation of our method. To facilitate understanding, we revisit the ControlNet-based latent

diffusion module. A pre-trained encoder, denoted as \mathcal{E} , processes an input image \mathbf{x}_0 , converting it from pixel space (with a height of H and a width of W) into latent space as \mathbf{z}_0

$$\mathbf{z}_0 = \mathcal{E}(\mathbf{x}_0), \mathbf{x}_0 \in \mathbb{R}^{H \times W \times 3}. \quad (1)$$

The diffusion process and the training objective function can be denoted by

$$\mathbf{z}_t = \sqrt{\bar{\alpha}_t} \mathbf{z}_0 + \sqrt{1 - \bar{\alpha}_t} \boldsymbol{\epsilon} \quad (2)$$

$$\mathcal{L} = \mathbb{E}_{\mathbf{z}, \boldsymbol{\epsilon} \sim \mathcal{N}(0, I), t \sim U(1, T)} [\|\boldsymbol{\epsilon} - \boldsymbol{\epsilon}_{\Theta}^t(\mathbf{z}_t; \mathbf{c}_f)\|_2^2]. \quad (3)$$

where $\boldsymbol{\epsilon}_{\Theta}^t(\mathbf{z}_t; \mathbf{c}_f)$ is the backbone with learnable parameters Θ and \mathbf{c}_f is the spatial condition from ControlNet.

3.2 Global Feature Compression Block

Global Feature Space

Given a dataset containing N nominal image samples, denoted as $\mathcal{X} = \{\mathbf{x}_1, \dots, \mathbf{x}_n, \dots, \mathbf{x}_N\}$, we utilize a pre-trained visual encoder \mathcal{F} to map the dataset into a d -dimensional global feature space \mathcal{D} in the following way

$$\mathcal{F} : \mathcal{X} \mapsto \mathcal{D}, \mathcal{D} = \{\mathbf{v}_n | \mathbf{v}_n \in \mathbb{R}^d, n = 1, 2, \dots, M\} \quad (4)$$

$$M = N \times \lfloor \frac{H}{m} \rfloor \times \lfloor \frac{W}{m} \rfloor \quad (5)$$

where $\mathbf{v}_n = \mathcal{F}(\mathbf{x}_n)$, and m indicates the downsampling ratio.

Coarse Feature Bank (CFB)

As the size of the dataset increases, the global feature space also becomes exceedingly large. Directly using the entire global feature space as a condition in a diffusion-based model is not feasible. Therefore, we perform a coarse compression on the global feature space through coresnet sampling to obtain a coarse feature bank. In Patchcore [Roth *et al.*, 2022], coresnet selection is applied to the global feature space with a certain ratio, such as 10%. Generally, to ensure the performance of anomaly detection, the coresnet sampling ratio is no less than 1%. However, even with this small ratio, the proposed "Memory Bank" [Roth *et al.*, 2022] still contains more than ten thousand samples, making it impractical to use as a condition input for a diffusion model. To address this issue, we set the number of samples in the Coarse Feature Bank as a fixed number ξ and we keep ξ no more than 1000 in our case. While it may suppress the performance of Patchcore, as auxiliary conditions in the model, a few hundred to a thousand samples are sufficient to be representative. The coarse compression is denoted by

$$\mathcal{S} : \mathcal{D} \mapsto \mathcal{B}_c, \mathcal{B}_c = \{\mathbf{v}_k | \mathbf{v}_k \in \mathbb{R}^d, k = 1, 2, \dots, \xi\} \quad (6)$$

where \mathcal{S} is the greedy coarse compression in [Roth *et al.*, 2022] and \mathcal{B}_c is the Coarse Feature Bank.

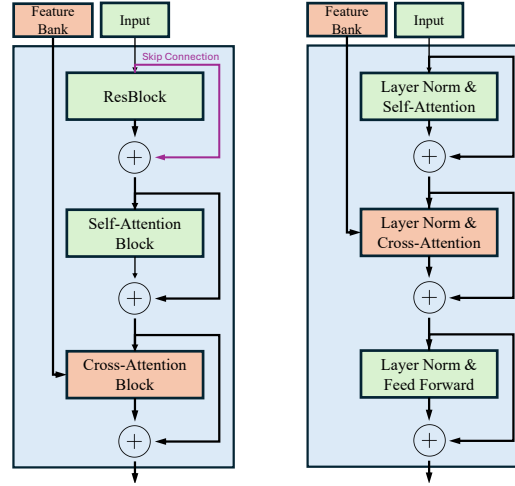
Fine Feature Bank (FFB)

Through the process in (6), CFB \mathcal{B}_c is feasible to serve as a global feature condition helping image reconstruction in the LDM backbone. However, during the image reconstruction process, unlike batch-wise training data samples, the \mathcal{B}_c introduced as the external condition in each iteration remains the same. Intuitively, we hope to select out the most relevant global feature information from the \mathcal{B}_c for each data sample. Inspired by the unsupervised methods such as K-NN in previous works and the encoder in LDM, we propose the concept of a Fine Feature Bank. The encoder \mathcal{E} in (1) and the pre-trained visual encoder \mathcal{F} in (4) share the same architecture and parameters to ensure consistency and efficient feature representation. As a result, besides the \mathcal{B}_c generated from (6), we can also generate a small batch-wise feature space \mathcal{D}_{bs} including ζ samples through (4) and (5). We then build a trainable Fine Compression Module (FCM) τ_θ mapping \mathcal{B}_c and \mathcal{D}_{bs} to Fine Feature Bank (FFB) via a multi-head cross-attention layer. We define $\mathbf{D}_{bs} \in \mathbb{R}^{\zeta \times d}$ as the vectorized \mathcal{D}_{bs} and $\mathbf{B}_c \in \mathbb{R}^{\xi \times d}$ as the vectorized \mathcal{B}_c .

$$\mathbf{Q} = \mathbf{D}_{bs}\theta_Q; \mathbf{K} = \mathbf{B}_c\theta_W; \mathbf{V} = \mathbf{B}_c\theta_V \quad (7)$$

$$\mathbf{B}_f = \tau_\theta(\mathcal{D}_{bs}, \mathcal{B}_c) = \text{softmax}\left(\frac{\mathbf{Q}\mathbf{K}^T}{\sqrt{d_k}}\right)\mathbf{V}\theta_B \in \mathbb{R}^{\zeta \times d} \quad (8)$$

where \mathbf{B}_f is the vectorized form of Fine Feature Bank (FFB) \mathcal{B}_f ; d_k is the scaling factor and $\theta := \{\theta_Q \in \mathbb{R}^{d \times d_k}, \theta_W \in \mathbb{R}^{d \times d_k}, \theta_V \in \mathbb{R}^{d \times d_k}, \theta_B \in \mathbb{R}^{d_k \times d}\}$ is the learnable parameter matrices [Vaswani *et al.*, 2017; Jaegle *et al.*, 2021]. To enable FFB or \mathcal{B}_c to serve as conditional inputs in the reconstruction process, we modified the U-Net backbone [Ronneberger *et al.*, 2015] architectures in DDAD and DiAD by introducing Global feature Conditioned Blocks (GCB) to support the input of global features as embedding conditions.



(a) GCB in CCAD(V) (b) GCB in CCAD (F & C)

Figure 3: Architecture of Global feature Conditioned Blocks.

3.3 Global feature Conditioned Diffusion Module

The Global feature Conditioned Diffusion Module (GCDM) is the main component of the reconstruction stream. It uses the Global Feature Conditioned Block (GCB) to integrate the global feature bank and refine the reconstruction quality. Corresponding to the different UNet structures in DDAD [Mousakan *et al.*, 2023] and DiAD [He *et al.*, 2024], we implement two variants of the Global Feature Conditioned Block (GCB). In DDAD, they employed a modified UNet in [Dhariwal and Nichol, 2021]. The network introduces attention blocks at 32x32, 16x16, and 8x8 resolutions. As shown in figure 3a, we add an extra cross-attention block following each corresponding combination of a ResBlock and Self-Attention Block. In DiAD, the external text embedding condition is integrated through the Basic Transformer Block, and we replace that module with the GCB in figure 3b instead. Based on the backbone structures in DDAD and DiAD, we propose three different CCAD variants, named as follows:

- CCAD with Fine Feature Bank, *i.e.*, CCAD(F)
- CCAD with Coarse Feature Bank, *i.e.*, CCAD(C)
- Vanilla CCAD, *i.e.*, CCAD(V)

In CCAD(F) and CCAD(C), similar to [Rombach *et al.*, 2022], the diffusion process and denoising process are conducted on the latent space. It uses a pre-trained Autoencoder [Esser *et al.*, 2021] to convert variables between pixel space and latent space. Same as [He *et al.*, 2024], CCAD(F) and CCAD(C) support multi-class anomaly detection tasks. In CCAD(V), the diffusion process and reconstruction process are conducted on the pixel space. Since no Batch-wise Feature Space can be obtained during the training process, we only utilize CFB \mathcal{B}_c as the global condition.

CCAD(F)

The Global Feature Conditioned Diffusion Module of CCAD(F) is shown in figure 2 which mainly contains the following components:

- Stable Diffusion Encoder Block (SDEB)

Table 1: Comparison of CCAD with state-of-the-art anomaly detection methods.

Method	Multi-class anomaly detection	Global Feature Utilized	Feature Space Compressed	Trainable Model	Minimal epochs eph required	AUC on MVTec-AD at eph
SPADE	No	Yes	No	-	-	0.850; 0.602
Pathcore	No	Yes	Reduced	-	-	0.858; 0.948
DDAD	No	No	-	UNet	1500	0.962; 0.966
DiAD	Yes	No	-	SGN [He <i>et al.</i> , 2024]	200	0.950; 0.954
CCAD(V)	No	Yes	Yes	GCDM	1000	0.963; 0.961
CCAD(C)	Yes	Yes	Yes	GCDM	100	0.958; 0.958
CCAD(F)	Yes	Yes	Yes	GCDM+ FCM	110	0.951; 0.961

- Stable Diffusion Middle Block (SDMB)
- Global Conditioned Encoder Block (GCEB)
- Global Conditioned Decoder Block (GCDB)

Both CCAD(F) and CCAD(C) use ControlNet [Zhang *et al.*, 2023b] as the main network for reconstruction, with GCB to grab useful information from the global feature bank. Given a certain image \mathbf{x} , Each denoising iteration can be formulated as:

$$\begin{aligned} \mathbf{z}_{t-1} = & \sqrt{\bar{\alpha}_{t-1}} \left(\frac{\mathbf{z}_t - \sqrt{1 - \bar{\alpha}_t} \epsilon_{\Theta}^t(\mathbf{z}_t; \mathbf{x}; \tau_{\Theta}(\mathcal{D}_{bs}; \mathcal{B}_c))}{\sqrt{\bar{\alpha}_t}} \right. \\ & \left. + \sqrt{1 - \bar{\alpha}_{t-1} - \sigma_t^2} \epsilon_{\Theta}^t(\mathbf{z}_t; \mathbf{x}; \tau_{\Theta}(\mathcal{D}_{bs}; \mathcal{B}_c)) \right. \\ & \left. + \sigma_t \epsilon_t. \right) \end{aligned} \quad (9)$$

The SDEB and SDMB consist of stacked diffusion blocks that are frozen during training. The GCEB and GCDB are composed of trainable GCBs. As shown in Figure 3b, each GCB includes a self-attention block to capture contextual information and a cross-attention block to extract and fuse relevant information from the global feature bank. objective function of the reconstruction process in CCAD can be denoted as:

$$\mathcal{L}_{CCAD(F)} = \mathbb{E}_{\mathbf{z}, \mathbf{x}, \epsilon, t} [\|\epsilon - \epsilon_{\Theta}^t(\mathbf{z}_t; \mathbf{x}; \tau_{\Theta}(\mathcal{D}_{bs}; \mathcal{B}_c))\|_2^2]. \quad (10)$$

The whole process in CCAD can be summarized in Appendix 1.

CCAD(C)

For tasks with a limited global feature space, our method supports directly using \mathcal{B}_c as the condition to enhance efficiency, which we denote as CCAD(C). CCAD(C) shares the same GCDM architecture as CCAD(F), with the key difference using another distinct pre-trained feature extractor to generate CFB \mathcal{B}_c . The objective function in CCAD(C) is changed from (10) to

$$\mathcal{L}_{CCAD(C)} = \mathbb{E}_{\mathbf{z}, \mathbf{x}, \epsilon, t} [\|\epsilon - \epsilon_{\Theta}^t(\mathbf{z}_t; \mathbf{x}; \mathcal{B}_c)\|_2^2]. \quad (11)$$

CCAD(V)

We also proposed a simplified CCAD version corresponding to the backbones in DDAD [Mousakhan *et al.*, 2023] as CCAD(V). The diffusion process is conducted directly on the pixel space by (17). Therefore, batch-wise feature space \mathcal{D}_{bs} is not available in the scenario and we only use \mathcal{B}_c as the global feature condition. Based on the structure proposed in [Dhariwal and Nichol, 2021], each module is trainable and

composed of ResNet Blocks and Self-attention layers. We then replace all the attention layers with our designed GCB in figure 3a. For the sampling process, derived from (18), when a target image $\bar{\mathbf{x}}_0$ is given and sample \mathbf{x}_{t-1} is generated from sample \mathbf{x}_t by

$$\begin{aligned} \mathbf{x}_{t-1} = & \sigma_t \epsilon_t + \sqrt{\bar{\alpha}_{t-1}} \left(\frac{\mathbf{x}_t - \sqrt{1 - \bar{\alpha}_t} \epsilon_{\Theta}^t(\mathbf{x}_t; \bar{\mathbf{x}}_t; \mathcal{B}_c)}{\sqrt{\bar{\alpha}_t}} \right) \\ & + \sqrt{1 - \bar{\alpha}_{t-1} - \sigma_t^2} \epsilon_{\Theta}^t(\mathbf{x}_t; \bar{\mathbf{x}}_t; \mathcal{B}_c) \end{aligned} \quad (12)$$

$$\epsilon_{\Theta}^t(\mathbf{x}_t; \bar{\mathbf{x}}_t; \mathcal{B}_c) = \epsilon_{\Theta}^t(\mathbf{x}_t; \mathcal{B}_c) - w \sqrt{1 - \bar{\alpha}_t} (\bar{\mathbf{x}}_t - \mathbf{x}_t) \quad (13)$$

$$\bar{\mathbf{x}}_t = \sqrt{\bar{\alpha}_t} \bar{\mathbf{x}}_0 + \sqrt{1 - \bar{\alpha}_t} \epsilon_{\Theta}^t(\mathbf{x}_t; \mathcal{B}_c) \quad (14)$$

where $\epsilon_{\Theta}^t(\mathbf{x}_t; \mathcal{B}_c)$ is the backbone with learnable parameters Θ . The objective function in CCAD(V) is denoted by

$$\mathcal{L}_{CCAD(V)} = \mathbb{E}_{\mathbf{x}, \epsilon, t} [\|\epsilon - \epsilon_{\Theta}^t(\mathbf{x}_t; \mathcal{B}_c)\|_2^2]. \quad (15)$$

Anomaly Detection

Similar to the method in [He *et al.*, 2024], in the inference phase, given a reconstructed image $\hat{\mathbf{x}}_0$, we compare the cosine similarity of the two images on the feature domain using a pre-trained feature extractor ψ on ImageNet [Deng *et al.*, 2009] to obtain the overall anomaly score \mathbf{M} . The calculation process can be denoted by

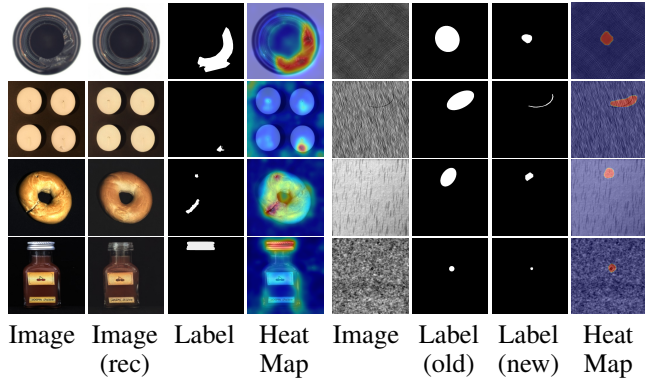
$$\mathbf{M} = \sum_l \sigma_l (1 - \frac{\psi_l(\mathbf{x}_0) \cdot \psi_l(\hat{\mathbf{x}}_0)}{\|\psi_l(\mathbf{x}_0)\| \|\psi_l(\hat{\mathbf{x}}_0)\|}) \quad (16)$$

where σ_l is the upsampling factor and l is the layer index of feature extractor ψ .

4 Experimental Results and Analysis

4.1 Datasets

We conduct experiments on MVTec-AD [Bergmann *et al.*, 2019; Bergmann *et al.*, 2021], VisA [Zou *et al.*, 2022], MVTec-3D [Bergmann *et al.*, 2022b], MVTec-loco [Bergmann *et al.*, 2022a], MTD [Huang *et al.*, 2018] and we annotated DAGM [Wieler *et al.*, 2007]. For MVTec-AD, VisA, MVTec-3d and MTD datasets, we use the original training and testing set as our training and testing data respectively. For MVTec-loco, we only use the RGB training and testing images in our experiment.



(a) Visualization of CCAD on various datasets (b) Annotation comparison on DAGM dataset

Figure 4: Qualitative example visualization.

4.2 New annotations on DAGM

The original DAGM [Wieler *et al.*, 2007] is a synthetic dataset on textured surfaces. It contains ten categories including 15000 non-defective images and 2100 defective images. However, only rough ellipses are provided as weak labels indicating the defective areas. As a result, DAGM has consistently performed poorly on pixel-level anomaly detection across various algorithms. For a long time, the DAGM dataset has been considered unsuitable for pixel-level anomaly localization tasks. To address this issue, we re-annotated 4 categories in the DAGM dataset (class 1 defect, class 2 scratch, class 7 blur, and class 9 spots). Compared with the previous elliptical ground truth, our provided labels feature more complicated contours, resulting in better pixel-level performance using the same algorithms. We then sampled 300 normal training images from each fine-grained annotated category as the training data. For the testing data, we sampled 75 normal and all defective images in each category as the testing data.

4.3 Evaluation Metrics

Same as the prior works, we use AUROC (Area Under the Receiver Operating Characteristic Curve), F1-score-max, and Average Precision to evaluate the performance of both class-level anomaly detection and pixel-level anomaly localization.

4.4 Implement details

We conduct each algorithm on multiple datasets with different hyperparameter settings. We also list the hyperparameter setting and source codes in Appendix E

SPADE [Cohen and Hoshen, 2020]

We implement SPADE on MVTec dataset [Bergmann *et al.*, 2019] using WideResNet50-2 [Zagoruyko and Komodakis, 2016] as the backbone and set the $k = 5$ in the k-NN algorithm.

PatchCore [Roth *et al.*, 2022]

We choose the encoder \mathcal{E} [Esser *et al.*, 2021] in LDM [Rombach *et al.*, 2022] as the backbone and resize all images into 256×256 pixels as inputs. select feature maps after the Res-Blocks in the third and fourth downsampling blocks to build

the global feature space. To ensure fairness, we set the number of samples in the Memory Bank in [Roth *et al.*, 2022] as 1000.

CCAD(V) and DDAD [Mousakhan *et al.*, 2023]

We implement DDAD and CCAD(V) on all the datasets. We completed the three steps including U-Nets training, feature extractor fine-tuning, and anomaly detection for each category respectively. To ensure a fair comparison, for a certain category, the two algorithms share the same training epochs, learning rate, and fine-tuned feature extractor. The only difference is the introduction of CFB \mathcal{B}_c as the conditioning input in our CCAD(V). The samples in the \mathcal{B}_c are generated by the feature maps from the second and the third stage of the residual blocks in a WideResNet50 [Zagoruyko and Komodakis, 2016] pre-trained on ImageNet [Deng *et al.*, 2009].

CCAD(C & F) and DiAD [He *et al.*, 2024]

We also conduct our CCAD (C & F) and DiAD on all the datasets we listed. For all the backbones in these three algorithms, we use the pre-trained Diffusion v1.5 model for initialization and we implement anomaly detection and localization on a ResNet50 pre-trained on ImageNet which is also shared among the three algorithms to ensure fairness. In CCAD(F), to mask sure that elements in batch-wise feature space \mathcal{D}_{bs} and CFB \mathcal{B}_c come from the same distribution, we choose the same feature maps as used in our PatchCore experiments to generate \mathcal{D}_{bs} and \mathcal{B}_c . In CCAD(C). Since only \mathcal{B}_c is introduced as the condition, we choose the feature maps from the second and the third stage of the residual blocks in a WideResNet50 [Zagoruyko and Komodakis, 2016] pre-trained on ImageNet [Deng *et al.*, 2009].

4.5 Comparison with the state-of-the-art

Shown in table 2, 3 and 4, we compare our CCAD with SOTA methods on all the datasets we listed. Our algorithm demonstrates a performance advantage across various datasets. From table 2, we found that although PatchCore still performs well on several categories with a memory bank including as few as 1000 samples, its AUC decreases greatly on many categories and datasets. It indicates that for an unsupervised learning anomaly detection approach based on global representation, the performance is highly dependent on the size of the global feature bank and whether there is a domain gap in the pre-trained feature extractor. CCAD(V) outperforms DDAD in most categories, both in class-level AUC and pixel-level AUC. Comparing with DiAD, the UNet backbone in DDAD is relatively simple and there is no additional conditional mechanism designed in the UNet backbone. As a result, the GCB in CCAD(V) makes a significant contribution to the reconstruction of normal images, which enables CCAD(V) to comprehensively outperform DDAD. We found that CCAD(C) even outperforms CCAD(F) in some categories, which is likely due to the reason that the global features extracted by the pre-trained WideResNet50 are more representative compared to those extracted by the encoder in LDM.

4.6 Ablation Studies

Shown in table 5, we compare CCAD(V) with different samples ξ in CFB \mathcal{B}_c . Surprisingly, even with a ξ of only 10,

Table 2: AUROC(Class-level; Pixel-level) comparison with SOTA methods on MVTec-AD [Bergmann *et al.*, 2019]. We highlighted the best result(s) in bold.

AUC \ Class	Algorithm	Single class based				Multi-class based		
		SPADE	PatchCore	DDAD	CCAD(V)	DiAD	CCAD(C)	CCAD(F)
Bottle		0.972; 0.562	0.995; 0.979	0.816; 0.878	0.975; 0.939	0.996; 0.984	1.000; 0.986	0.998; 0.986
Cable		0.791; 0.654	0.664; 0.906	0.947; 0.965	0.959 ; 0.960	0.850; 0.883	0.832; 0.900	0.904 ; 0.929
Capsule		0.897; 0.638	0.852; 0.898	0.909; 0.928	0.943; 0.961	0.891; 0.963	0.916; 0.959	0.899; 0.965
Carpet		0.928; 0.633	0.941; 0.971	0.877; 0.926	0.898; 0.941	0.990; 0.982	0.993; 0.987	0.992 ; 0.987
Grid		0.471; 0.566	0.769; 0.978	0.999; 0.993	1.000 ; 0.993	0.949; 0.947	0.945; 0.930	0.995 ; 0.990
Hazelnut		0.881; 0.830	0.937; 0.974	0.937; 0.973	0.941; 0.979	0.971; 0.973	0.972; 0.972	0.977 ; 0.981
Leather		0.954; 0.615	0.988; 0.994	0.907; 0.984	0.928; 0.987	1.000 ; 0.991	1.000; 0.979	1.000 ; 0.990
Metal Nut		0.710; 0.509	0.727; 0.964	0.991; 0.982	1.000 ; 0.985	0.987 ; 0.978	0.971; 0.978	0.978; 0.971
Pill		0.803; 0.647	0.864; 0.967	0.957; 0.972	0.965 ; 0.974	0.911; 0.962	0.942; 0.964	0.942; 0.959
Screw		0.667; 0.583	0.543; 0.967	0.964; 0.992	0.967 ; 0.992	0.879 ; 0.969	0.881; 0.975	0.864 ; 0.976
Tile		0.965; 0.632	0.933; 0.953	1.000 ; 0.979	1.000 ; 0.979	0.965; 0.926	0.966; 0.923	0.983; 0.929
Toothbrush		0.889; 0.568	0.917; 0.986	0.981; 0.985	1.000 ; 0.984	0.994; 0.990	0.961; 0.989	0.975; 0.962
Transistor		0.903; 0.507	0.778; 0.756	0.947; 0.880	0.960 ; 0.894	0.945; 0.899	0.992; 0.955	0.971; 0.921
Wood		0.959; 0.644	0.968; 0.941	0.992; 0.944	0.998 ; 0.931	0.982; 0.918	0.987; 0.930	0.987 ; 0.932
Zipper		0.966; 0.415	0.995 ; 0.987	0.979; 0.955	0.987; 0.975	0.938; 0.948	0.933; 0.960	0.954 ; 0.959
mean		0.850; 0.602	0.858; 0.948	0.943; 0.956	0.968 ; 0.965	0.950; 0.954	0.953; 0.959	0.961 ; 0.962

Table 3: Average AUROC(Class-level; Pixel-level) comparison with SOTA methods on other datasets.

Dataset	PatchCore	DDAD	CCAD(V)	DiAD	CCAD(C)	CCAD(F)
VisA	0.761; 0.923	0.963; 0.958	0.978 ; 0.957	0.742 ; 0.898	0.651; 0.906	0.735; 0.895
MVTec-3d	0.67; 0.697	0.755; 0.890	0.779 ; 0.935	0.709 ; 0.957	0.709 ; 0.971	0.683; 0.938
MVTec-loco	0.654; 0.643	0.886; 0.678	0.897 ; 0.690	0.665; 0.714	0.671 ; 0.718	0.670; 0.715
MTD	0.575; 0.5895	0.934 ; 0.719	0.897; 0.755	0.966; 0.820	0.959; 0.826	0.968 ; 0.818

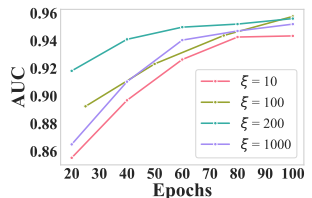
Table 5: AUROC(Class-level; Pixel-level) on MVTec with different ξ in CCAD(V).

AUC \ Class	Algorithm	CCAD(V)		
		$\xi = 0$	$\xi = 10$	$\xi = 200$
bottle		0.816; 0.878	0.976 ; 0.939	0.975; 0.939
cable		0.947; 0.965	0.960; 0.966	0.959 ; 0.960
capsule		0.909; 0.928	0.943 ; 0.961	0.943 ; 0.961
carpet		0.877; 0.926	0.891; 0.928	0.898 ; 0.941
grid		0.999; 0.993	1.000 ; 0.993	1.000 ; 0.993
hazelnut		0.937; 0.973	0.982 ; 0.971	0.941; 0.979
leather		0.907; 0.984	0.963 ; 0.989	0.928; 0.987
metal		0.991; 0.982	0.999; 0.982	1.000 ; 0.985
pill		0.957; 0.972	0.967 ; 0.987	0.965; 0.974
screw		0.964; 0.992	0.975 ; 0.993	0.967; 0.992
tile		1.000 ; 0.979	1.000 ; 0.979	1.000 ; 0.979
toothbrush		0.981; 0.985	0.994; 0.984	1.000 ; 0.984
transistor		0.947; 0.880	0.952; 0.893	0.960 ; 0.894
wood		0.992; 0.944	0.997; 0.930	0.998 ; 0.931
zipper		0.979; 0.955	0.979; 0.973	0.987 ; 0.975
mean		0.943; 0.956	0.971 ; 0.963	0.968; 0.965

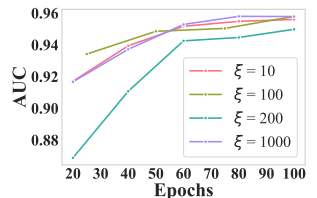
CCAD already outperforms DDAD, and as the dimension increases, there is no clear upward trend in AUC. This is likely because the GCBs, as learnable blocks embedding in the U-Net at each layer, can selectively utilize representative global feature information through the cross-attention layer during training. Even ξ is small, the available information learned by GVBs is already sufficient for nominal image reconstruction. Additionally, since our algorithm performs well on MVTec, the potential for AUC improvement as dimension

Table 4: AUROC(Class-level; Pixel-level) comparison with SOTA methods on our new annotated DAGM2007 dataset.

Class	DDAD	CCAD(V)	DiAD	CCAD(C)	CCAD(F)
class 1	0.646; 0.882	0.669 ; 0.886	0.588; 0.789	0.584; 0.806	0.613 ; 0.830
class 2	1.000 ; 0.992	1.000 ; 0.993	0.937; 0.970	0.988; 0.991	0.991 ; 0.992
class 7	0.973; 0.991	0.985 ; 0.992	0.586; 0.787	0.627; 0.799	0.747 ; 0.899
class 9	0.907; 0.973	0.925 ; 0.982	0.941; 0.993	0.910; 0.995	0.947 ; 0.996
mean	0.882; 0.960	0.895 ; 0.963	0.763; 0.885	0.777; 0.898	0.824 ; 0.929



(a) Class-wise AUC on MVTec with different ξ



(b) Pixel-wise AUC on MVTec with different ξ

sionality increases is inherently limited. We also compare CCAD(C) with different ξ on MVTec. Shown in figure 5a and 5b, when ξ is set to 10, the AUC is at its lowest, while the best AUC is achieved with ξ of 100 and 200. However, no significant AUC improvement is observed when ξ is set to 1000. This indicates that with $\xi = 100$, the \mathcal{B}_c is already sufficient to aid in image reconstruction.

4.7 Faster Convergence in CCAD

We also compare the convergence speed of DDAD, DiAD, and CCAD in table 2. CCAD significantly outperforms DDAD and DiAD in speed while achieving a relatively high AUC performance. A significant reason for this phenomenon is that, in the early stages of model training, the global information from the condition provides a great contribution to model learning, and enables the reconstructed images to retain features from the training data. We demonstrate more

experimental results and analysis in the appendix

4.8 New annotated labels

Shown in figure 4b, our new annotated ground truth is qualitatively more aligned with the anomaly maps in terms of both outlines and locations indicating that our annotated labels are more proper and accurate. We demonstrate the results and analysis in the appendix.

5 Conclusion

In this paper, we proposed CCAD: Anomaly Detection Conditioned on Compressed Global Feature Space that uses a two-stage coarse-to-fine approach converting global features as conditions for image reconstruction on anomaly detection tasks. Extensive experimental results show that CCAD exhibits a notable advantage over SOTA algorithm across multiple datasets. We also re-annotated the DAGM2007 dataset [Wieler *et al.*, 2007], providing more reliable and accurate labels.

References

[Akcay *et al.*, 2019] Samet Akcay, Amir Atapour-Abarghouei, and Toby P Breckon. Ganomaly: Semi-supervised anomaly detection via adversarial training. In *Computer Vision–ACCV 2018: 14th Asian Conference on Computer Vision, Perth, Australia, December 2–6, 2018, Revised Selected Papers, Part III 14*, pages 622–637. Springer, 2019.

[Batzner *et al.*, 2024] Kilian Batzner, Lars Heckler, and Rebecca König. Efficientad: Accurate visual anomaly detection at millisecond-level latencies. In *Proceedings of the IEEE/CVF Winter Conference on Applications of Computer Vision (WACV)*, pages 128–138, January 2024.

[Bergman *et al.*, 2020] Liron Bergman, Niv Cohen, and Yedid Hoshen. Deep nearest neighbor anomaly detection. *arXiv preprint arXiv:2002.10445*, 2020.

[Bergmann *et al.*, 2019] Paul Bergmann, Michael Fauser, David Sattlegger, and Carsten Steger. Mvtec ad — a comprehensive real-world dataset for unsupervised anomaly detection. In *2019 IEEE/CVF Conference on Computer Vision and Pattern Recognition (CVPR)*, pages 9584–9592, 2019.

[Bergmann *et al.*, 2020] Paul Bergmann, Michael Fauser, David Sattlegger, and Carsten Steger. Uninformed students: Student-teacher anomaly detection with discriminative latent embeddings. In *Proceedings of the IEEE/CVF conference on computer vision and pattern recognition*, pages 4183–4192, 2020.

[Bergmann *et al.*, 2021] Paul Bergmann, Kilian Batzner, Michael Fauser, David Sattlegger, and Carsten Steger. The mvtec anomaly detection dataset: A comprehensive real-world dataset for unsupervised anomaly detection. *International Journal of Computer Vision*, 129(4):1038–1059, 2021.

[Bergmann *et al.*, 2022a] Paul Bergmann, Kilian Batzner, Michael Fauser, David Sattlegger, and Carsten Steger. Beyond dents and scratches: Logical constraints in unsupervised anomaly detection and localization. *International Journal of Computer Vision*, 130, 04 2022.

[Bergmann *et al.*, 2022b] Paul Bergmann, Xin Jin, David Sattlegger, and Carsten Steger. The mvtec 3d-ad dataset for unsupervised 3d anomaly detection and localization. In *the 17th International Joint Conference on Computer Vision, Imaging and Computer Graphics Theory and Application*, volume 5, 2022.

[Cohen and Hoshen, 2020] Niv Cohen and Yedid Hoshen. Sub-image anomaly detection with deep pyramid correspondences. *arXiv preprint arXiv:2005.02357*, 2020.

[Defard *et al.*, 2021] Thomas Defard, Aleksandr Setkov, Angelique Loesch, and Romaric Audigier. Padim: a patch distribution modeling framework for anomaly detection and localization. In *International Conference on Pattern Recognition*, pages 475–489. Springer, 2021.

[Deng *et al.*, 2009] Jia Deng, Wei Dong, Richard Socher, Li-Jia Li, Kai Li, and Li Fei-Fei. Imagenet: A large-scale hierarchical image database. In *2009 IEEE Conference on Computer Vision and Pattern Recognition*, pages 248–255, 2009.

[Dhariwal and Nichol, 2021] Prafulla Dhariwal and Alexander Quinn Nichol. Diffusion models beat GANs on image synthesis. In A. Beygelzimer, Y. Dauphin, P. Liang, and J. Wortman Vaughan, editors, *Advances in Neural Information Processing Systems*, 2021.

[Esser *et al.*, 2021] Patrick Esser, Robin Rombach, and Björn Ommer. Taming transformers for high-resolution image synthesis. In *Proceedings of the IEEE/CVF conference on computer vision and pattern recognition*, pages 12873–12883, 2021.

[He *et al.*, 2016] Kaiming He, Xiangyu Zhang, Shaoqing Ren, and Jian Sun. Deep residual learning for image recognition. In *2016 IEEE Conference on Computer Vision and Pattern Recognition (CVPR)*, pages 770–778, 2016.

[He *et al.*, 2024] Haoyang He, Jiangning Zhang, Hongxu Chen, Xuhai Chen, Zhishan Li, Xu Chen, Yabiao Wang, Chengjie Wang, and Lei Xie. A diffusion-based framework for multi-class anomaly detection. In *Proceedings of the AAAI Conference on Artificial Intelligence*, volume 38, pages 8472–8480, 2024.

[Ho *et al.*, 2020] Jonathan Ho, Ajay Jain, and Pieter Abbeel. Denoising diffusion probabilistic models. In H. Larochelle, M. Ranzato, R. Hadsell, M.F. Balcan, and H. Lin, editors, *Advances in Neural Information Processing Systems*, volume 33, pages 6840–6851. Curran Associates, Inc., 2020.

[Huang *et al.*, 2018] Yibin Huang, Congying Qiu, Yue Guo, Xiaonan Wang, and Kui Yuan. Surface defect saliency of magnetic tile. In *2018 IEEE 14th International Conference on Automation Science and Engineering (CASE)*, pages 612–617, 2018.

[Hyun *et al.*, 2024] Jeeho Hyun, Sangyun Kim, Giyoung Jeon, Seung Hwan Kim, Kyunghoon Bae, and Byung Jun Kang. Reconpatch : Contrastive patch representation learning for industrial anomaly detection. In *2024 IEEE/CVF Winter Conference on Applications of Computer Vision (WACV)*, pages 2041–2050, 2024.

[Jaegle *et al.*, 2021] Andrew Jaegle, Felix Gimeno, Andy Brock, Oriol Vinyals, Andrew Zisserman, and Joao Carreira. Perceiver: General perception with iterative attention. In *International conference on machine learning*, pages 4651–4664. PMLR, 2021.

[Mousakhan *et al.*, 2023] Arian Mousakhan, Thomas Brox, and Jawad Tayyub. Anomaly detection with conditioned denoising diffusion models. *arXiv preprint arXiv:2305.15956*, 2023.

[Rombach *et al.*, 2022] Robin Rombach, Andreas Blattmann, Dominik Lorenz, Patrick Esser, and Björn Ommer. High-resolution image synthesis with latent diffusion models. In *Proceedings of the IEEE/CVF Conference on Computer Vision and Pattern Recognition*, pages 10684–10695, 2022.

[Ronneberger *et al.*, 2015] Olaf Ronneberger, Philipp Fischer, and Thomas Brox. U-net: Convolutional networks for biomedical image segmentation. In Nassir Navab, Joachim Hornegger, William M. Wells, and Alejandro F. Frangi, editors, *Medical Image Computing and Computer-Assisted Intervention – MICCAI 2015*, pages 234–241, Cham, 2015. Springer International Publishing.

[Roth *et al.*, 2022] Karsten Roth, Latha Pemula, Joaquin Zepeda, Bernhard Schölkopf, Thomas Brox, and Peter Gehler. Towards total recall in industrial anomaly detection. In *2022 IEEE/CVF Conference on Computer Vision and Pattern Recognition (CVPR)*, pages 14298–14308, 2022.

[Song *et al.*, 2020] Jiaming Song, Chenlin Meng, and Stefano Ermon. Denoising diffusion implicit models. *arXiv preprint arXiv:2010.02502*, 2020.

[Vaswani *et al.*, 2017] Ashish Vaswani, Noam Shazeer, Niki Parmar, Jakob Uszkoreit, Llion Jones, Aidan N Gomez, Łukasz Kaiser, and Illia Polosukhin. Attention is all you need. *Advances in neural information processing systems*, 30, 2017.

[Wang *et al.*, 2024] Shuyuan Wang, Qi Li, Huiyuan Luo, Chengkan Lv, and Zhengtao Zhang. Produce once, utilize twice for anomaly detection. *IEEE Transactions on Circuits and Systems for Video Technology*, 2024.

[Wieler *et al.*, 2007] Matthias Wieler, Tobias Hahn, and Fred A. Hamprecht. Weakly Supervised Learning for Industrial Optical Inspection. *Zenodo*, September 2007.

[Wyatt *et al.*, 2022] Julian Wyatt, Adam Leach, Sebastian M. Schmon, and Chris G. Willcocks. Anoddpm: Anomaly detection with denoising diffusion probabilistic models using simplex noise. In *2022 IEEE/CVF Conference on Computer Vision and Pattern Recognition Workshops (CVPRW)*, pages 649–655, 2022.

[Yi and Yoon, 2020] Jihun Yi and Sungroh Yoon. Patch svdd: Patch-level svdd for anomaly detection and segmentation. In *Proceedings of the Asian conference on computer vision*, 2020.

[Zagoruyko and Komodakis, 2016] Sergey Zagoruyko and Nikos Komodakis. Wide residual networks. In *Proceedings of the British Machine Vision Conference 2016*. British Machine Vision Association, 2016.

[Zhang *et al.*, 2023a] Hui Zhang, Zheng Wang, Zuxuan Wu, and Yu-Gang Jiang. Diffusionad: Denoising diffusion for anomaly detection. *arXiv preprint arXiv:2303.08730*, 4, 2023.

[Zhang *et al.*, 2023b] Lvmin Zhang, Anyi Rao, and Maneesh Agrawala. Adding conditional control to text-to-image diffusion models. In *Proceedings of the IEEE/CVF International Conference on Computer Vision (ICCV)*, pages 3836–3847, October 2023.

[Zou *et al.*, 2022] Yang Zou, Jongheon Jeong, Latha Pemula, Dongqing Zhang, and Onkar Dabeer. Spot-the-difference self-supervised pre-training for anomaly detection and segmentation. In *European Conference on Computer Vision*, pages 392–408. Springer, 2022.

Supplementary Material

List of Abbreviation and Symbols

\bar{x}	Target image in DDAD and CCAD(V)
ϵ	Noise in diffusion process
ϵ_Θ	Diffusion model trainable backbones
$\mathcal{D}/\mathcal{D}_{bs}$	Global Feature Space / Batch-wise Feature Space
\mathcal{E}	Pre-trained latent encoder in LDM
\mathcal{F}	Pre-trained visual encoder
$\mathcal{L}(\cdot)$	Objective function
ψ	Pre-trained feature extractor from anomaly detection
σ	upsampling factor
\mathbf{M}	Anomaly Score
\mathbf{v}	Samples in Feature Banks
\mathbf{x}/\mathcal{X}	Training / Testing data (images)
\mathbf{z}	Training / Testing input in latent space
ξ	Number of samples in \mathcal{B}_c
t	time step in diffusion process
CFB, \mathcal{B}_c	Coarse Feature Bank
FCM, τ_θ	Fine Compression Module
FFB, \mathcal{B}_f	Fine Feature Bank
GCB	Global feature Conditioned Block
GCDB	Global feature Conditioned Decoder Blocks
GCDM	Global feature Conditioned Diffusion Module
GCEB	Global feature Conditioned Encoder Blocks
SDEB	Stable Diffusion Encoder Blocks
SDMB	Stable Diffusion Middlle Blocks

A Preliminary of Diffusion Model

In this section, we introduce some preliminary knowledge related to diffusion models, which serves as the foundation for the equations we derived. For an input image \mathbf{x}_0 , the diffusion process of DDPM [Ho *et al.*, 2020] can be denoted by

$$\mathbf{x}_t = \sqrt{\bar{\alpha}_t} \mathbf{x}_0 + \sqrt{1 - \bar{\alpha}_t} \epsilon, \quad \bar{\alpha}_t = \prod_{i=1}^t \alpha_i, \quad \epsilon \sim \mathcal{N}(0, \mathbf{I}) \quad (17)$$

where $\alpha_i = 1 - \beta_i$ and $\{\beta_i | i = 1, \dots, t\}$ is a pre-defined variance schedule. In DDIM [Song *et al.*, 2020], for the sampling process, a sample \mathbf{x}_{t-1} is generated from sample \mathbf{x}_t by

$$\mathbf{x}_{t-1} = \sqrt{\bar{\alpha}_{t-1}} \left(\frac{\mathbf{x}_t - \sqrt{1 - \bar{\alpha}_t} \epsilon_\Theta^t(\mathbf{x}_t)}{\sqrt{\bar{\alpha}_t}} \right) + \sqrt{1 - \bar{\alpha}_{t-1} - \sigma_t^2} \epsilon_\Theta^t(\mathbf{x}_t) + \sigma_t \epsilon_t \quad (18)$$

where σ_t is the value determining the randomness in the sampling process.

B Frameworks of CCAD(C & V)

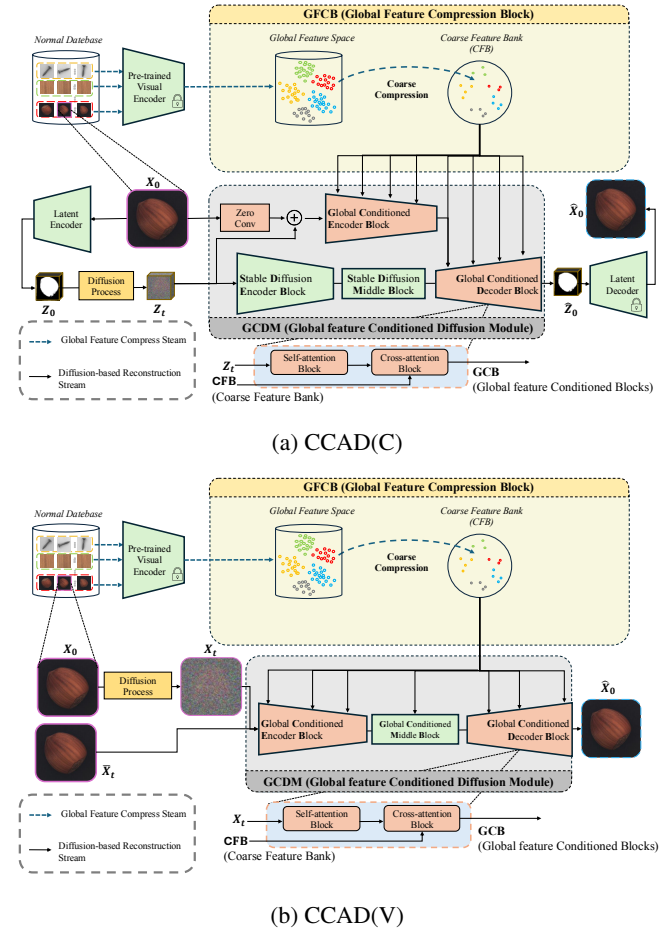


Figure 6: The frameworks of CCAD(C & V)

The framework of CCAD(C) is shown in figure 6a. Unlike the framework in figure 2, we replace the FFB with CFB. The framework of CCAD(V) is shown in figure 6b. The diffusion process is conducted on the pixel space and we only implement a backbone consisting of GCEB and GCDB to reconstruction images

C The complete algorithm of CCAD

In this section, we list the pseudo-code of our CCAD algorithm

Algorithm 1 CCAD(F) (Training and Reconstruction)

Input: $\mathcal{B}_c, \mathcal{X}$
Pre-trained Autoencoder: \mathcal{E}, \mathcal{D}
Trainable Model: $\tau_\theta; \epsilon_\Theta$

```

1: repeat
2:    $\mathbf{x} \sim \mathcal{X}, \mathbf{z} = \mathcal{E}(\mathbf{x}), t \sim U(1, T),$ 
    $\epsilon \sim \mathcal{N}(0, \mathbf{I})$ 
3:    $\mathbf{z}_t = \sqrt{\bar{\alpha}_t} \mathbf{z}_0 + \sqrt{1 - \bar{\alpha}_t} \epsilon$ 
4:   Generate  $\mathcal{D}_{bs}$ 
5:    $\min_{\Theta, \theta} \|\epsilon - \epsilon_\Theta^t(\mathbf{z}_t; \mathbf{x}; \tau_\theta(\mathcal{D}_{bs}; \mathcal{B}_c))\|_2^2$ 
6: until converged

7: for  $\mathbf{x}_i$  in  $\mathcal{X}$  do
8:    $\mathbf{z}_T \sim \mathcal{N}(0, \mathbf{I})$ 
9:   for  $t = T, \dots, 1$  do
10:    sample  $\mathbf{z}_{t-1}$  through (9)
11:   end for
12:    $\hat{\mathbf{x}}_i = \mathcal{D}(\mathbf{z}_0)$ 
13: end for
14: return  $\hat{\mathcal{X}} = \{\hat{\mathbf{x}}_i\}$ 

```

Similar as equation (9), we define the sampling equation in CCAD(C) as

$$\begin{aligned} \mathbf{z}_{t-1} = & \sqrt{\bar{\alpha}_{t-1}} \left(\frac{\mathbf{z}_t - \sqrt{1 - \bar{\alpha}_t} \epsilon_\Theta^t(\mathbf{z}_t; \mathbf{x}; \mathcal{B}_c)}{\sqrt{\bar{\alpha}_t}} \right) \\ & + \sqrt{1 - \bar{\alpha}_{t-1} - \sigma_t^2} \epsilon_\Theta^t(\mathbf{z}_t; \mathbf{x}; \mathcal{B}_c) \\ & + \sigma_t \epsilon_t. \end{aligned} \quad (19)$$

The pseudo-code of CCAD(C) can be denoted by

Algorithm 2 CCAD(C) (Training and Reconstruction)

Input: $\mathcal{B}_c, \mathcal{X}$
Pre-trained Autoencoder: \mathcal{E}, \mathcal{D}
Trainable Model: ϵ_Θ

```

1: repeat
2:    $\mathbf{x} \sim \mathcal{X}, \mathbf{z} = \mathcal{E}(\mathbf{x}), t \sim U(1, T),$ 
    $\epsilon \sim \mathcal{N}(0, \mathbf{I})$ 
3:    $\mathbf{z}_t = \sqrt{\bar{\alpha}_t} \mathbf{z}_0 + \sqrt{1 - \bar{\alpha}_t} \epsilon$ 
4:    $\min_{\Theta} \|\epsilon - \epsilon_\Theta^t(\mathbf{z}_t; \mathbf{x}; \mathcal{B}_c)\|_2^2$ 
5: until converged

6: for  $\mathbf{x}_i$  in  $\mathcal{X}$  do
7:    $\mathbf{z}_T \sim \mathcal{N}(0, \mathbf{I})$ 
8:   for  $t = T, \dots, 1$  do
9:    sample  $\mathbf{z}_{t-1}$  through (19)
10:   end for
11:    $\hat{\mathbf{x}}_i = \mathcal{D}(\mathbf{z}_0)$ 
12: end for
13: return  $\hat{\mathcal{X}} = \{\hat{\mathbf{x}}_i\}$ 

```

The pseudo-code of CCAD(V) can be denoted by

Algorithm 3 CCAD(V) (Training and Reconstruction)

Input: $\mathcal{B}_c, \mathcal{X}$
Trainable Model: ϵ_Θ

```

1: repeat
2:    $\mathbf{x}_0 \sim \mathcal{X}, t \sim U(1, T), \epsilon \sim \mathcal{N}(0, \mathbf{I})$ 
3:    $\mathbf{x}_t = \sqrt{\bar{\alpha}_t} \mathbf{x}_0 + \sqrt{1 - \bar{\alpha}_t} \epsilon$ 
4:    $\min_{\Theta} \|\epsilon - \epsilon_\Theta^t(\mathbf{x}_t; \mathcal{B}_c)\|_2^2$ 
5: until converged

6: for  $\bar{\mathbf{x}}_i$  in  $\mathcal{X}$  do
7:    $\mathbf{x}_T \sim \mathcal{N}(0, \mathbf{I})$ 
8:   for  $t = T, \dots, 1$  do
9:    sample  $\mathbf{x}_{t-1}$  by (12)
10:   end for
11:    $\hat{\mathbf{x}}_i = \mathbf{x}_0$ 
12: end for
13: return  $\hat{\mathcal{X}} = \{\hat{\mathbf{x}}_i\}$ 

```

D Additional Details on Experiment

We list more experimental details in this section. The best result(s) are highlighted in bold.

D.1 MVTec Dataset

Table 6: F1 score (Class-level; Pixel-level) on MVTec-AD with DiAD, CCAD(C & F).

Class	DiAD	CCAD(C)	CCAD(F)
bottle	1.000 ; 0.750	1.000 ; 0.760	0.863; 0.119
cable	0.848; 0.389	0.854 ; 0.398	0.760; 0.105
capsule	0.944 ; 0.433	0.938; 0.437	0.905; 0.124
carpet	0.983 ; 0.566	0.967; 0.616	0.943; 0.532
grid	0.982 ; 0.147	0.982 ; 0.211	0.874; 0.019
hazelnut	0.929; 0.498	0.958 ; 0.484	0.904; 0.437
leather	1.000 ; 0.435	1.000 ; 0.465	0.961; 0.377
metal	0.961; 0.834	0.962 ; 0.839	0.894; 0.294
pill	0.953; 0.634	0.954 ; 0.646	0.916; 0.097
screw	0.907 ; 0.280	0.895; 0.216	0.869; 0.044
tile	0.959 ; 0.575	0.952; 0.578	0.921; 0.500
toothbrush	0.938; 0.544	0.952 ; 0.644	0.833; 0.092
transistor	0.975 ; 0.604	0.975 ; 0.614	0.571; 0.096
wood	0.968; 0.466	0.967; 0.467	0.975 ; 0.432
zipper	0.954 ; 0.516	0.954 ; 0.480	0.881; 0.074
mean	0.953; 0.511	0.954 ; 0.524	0.871; 0.223

Table 7: Average precision (Class-level; Pixel-level) on MVTec-AD with DiAD, CCAD(C & F).

Class	DiAD	CCAD(C)	CCAD(F)
bottle	1.000 ; 0.786	1.000 ; 0.790	0.703; 0.048
cable	0.920 ; 0.331	0.915; 0.347	0.623; 0.057
capsule	0.960; 0.405	0.981 ; 0.405	0.773; 0.062
carpet	0.997 ; 0.612	0.994; 0.630	0.987; 0.495
grid	0.965 ; 0.051	0.933; 0.082	0.914; 0.007
hazelnut	0.980 ; 0.492	0.976; 0.473	0.968; 0.403
leather	1.000 ; 0.423	1.000 ; 0.479	0.987; 0.341
metal	0.994 ; 0.848	0.993; 0.862	0.744; 0.168
pill	0.993 ; 0.657	0.992; 0.661	0.903; 0.056
screw	0.936 ; 0.171	0.896; 0.107	0.802; 0.022
tile	0.993 ; 0.500	0.991; 0.497	0.979; 0.435
toothbrush	0.941; 0.540	0.967 ; 0.640	0.802; 0.048
transistor	0.992 ; 0.535	0.990; 0.502	0.467; 0.051
wood	0.997 ; 0.431	0.995; 0.440	0.995; 0.395
zipper	0.984; 0.439	0.988 ; 0.394	0.760; 0.030
mean	0.977 ; 0.481	0.974; 0.487	0.823; 0.174

D.2 VisA Dataset

Table 8: AUROC(Class-level; Pixel-level) comparison with SOTA methods on VisA [Zou *et al.*, 2022]

AUC Class	Algorithm	Single class based			Multi-class based.		
		PatchCore	DDAD	CCAD(V)	DiAD	CCAD(C)	CCAD(F)
candle		0.717; 0.881	0.973; 0.982	0.979; 0.987	0.826; 0.951	0.846; 0.957	0.684; 0.938
cashew		0.851; 0.777	0.990; 0.847	0.988; 0.795	0.842 ; 0.806	0.812; 0.830	0.594; 0.947
capsules		0.688; 0.974	0.981; 0.996	0.986; 0.996	0.583; 0.951	0.527; 0.836	0.509; 0.793
chewinggum		0.925; 0.921	0.975; 0.886	0.999; 0.921	0.909; 0.920	0.878; 0.916	0.787; 0.912
fryum		0.769; 0.885	0.993; 0.947	0.999 ; 0.930	0.743; 0.782	0.773 ; 0.852	0.675; 0.923
macaroni1		0.785; 0.944	0.879; 0.969	0.945; 0.980	0.760; 0.928	0.733; 0.916	0.536; 0.884
macaroni2		0.472; 0.936	0.930; 0.994	0.916; 0.994	0.550; 0.849	0.524; 0.837	0.503; 0.841
pipe fryum		0.901; 0.920	0.903; 0.943	0.995 ; 0.938	0.943; 0.984	0.945; 0.986	0.636; 0.979
pcb1		0.730; 0.988	0.960; 0.992	0.971; 0.993	0.686; 0.920	0.723 ; 0.915	0.631; 0.889
pcb2		0.896; 0.971	0.972 ; 0.967	0.959; 0.973	0.740 ; 0.915	0.735; 0.923	0.670; 0.897
pcb3		0.701; 0.950	1.000; 0.982	1.000 ; 0.980	0.617 ; 0.933	0.599; 0.950	0.593; 0.948
pcb4		0.697; 0.934	0.999 ; 0.987	0.999; 0.991	0.737; 0.856	0.795 ; 0.857	0.792; 0.865
mean		0.761; 0.923	0.963; 0.958	0.978 ; 0.957	0.745 ; 0.900	0.741; 0.898	0.634; 0.901

Table 9: F1 score (Class-level; Pixel-level) on VisA with DiAD, CCAD(C & F).

F1	DiAD	CCAD(C)	CCAD(F)
candle	0.741; 0.220	0.788; 0.220	0.757; 0.180
cashew	0.868 ; 0.260	0.855; 0.454	0.861; 0.282
capsules	0.769; 0.291	0.769 ; 0.049	0.769 ; 0.185
chewinggum	0.876; 0.404	0.841; 0.481	0.884 ; 0.380
fryum	0.800; 0.232	0.803; 0.515	0.806 ; 0.233
macaroni1	0.688; 0.119	0.708; 0.129	0.727 ; 0.103
macaroni2	0.669; 0.021	0.667; 0.012	0.667; 0.021
pipe fryum	0.942 ; 0.478	0.898; 0.633	0.933; 0.486
pcb1	0.691 ; 0.105	0.677; 0.271	0.678; 0.127
pcb2	0.703; 0.084	0.747; 0.105	0.708; 0.085
pcb3	0.664 ; 0.129	0.664; 0.210	0.664 ; 0.146
pcb4	0.664; 0.134	0.746; 0.162	0.693; 0.161
mean	0.756; 0.206	0.763; 0.270	0.762; 0.199

Table 10: Average precision (Class-level; Pixel-level) on VisA with DiAD, CCAD(C & F).

AP	DiAD	CCAD(C)	CCAD(F)
candle	0.803; 0.116	0.846; 0.116	0.798; 0.075
cashew	0.935; 0.170	0.936; 0.361	0.948 ; 0.176
capsules	0.673; 0.157	0.593; 0.017	0.625; 0.094
chewinggum	0.953 ; 0.335	0.933; 0.391	0.943; 0.293
fryum	0.866; 0.165	0.902; 0.410	0.857; 0.163
macaroni1	0.719; 0.050	0.741; 0.080	0.753 ; 0.049
macaroni2	0.483; 0.007	0.463; 0.003	0.434; 0.004
pipe fryum	0.982 ; 0.413	0.961; 0.612	0.975; 0.425
pcb1	0.731; 0.044	0.769; 0.122	0.717; 0.055
pcb2	0.716; 0.027	0.787; 0.039	0.725; 0.028
pcb3	0.636; 0.043	0.692; 0.073	0.652; 0.052
pcb4	0.717; 0.068	0.832; 0.068	0.777; 0.067
mean	0.768; 0.133	0.788; 0.191	0.767; 0.123

D.3 MVTec-loco Dataset

Table 11: AUROC (Class-level; Pixel-level) comparison with SOTA methods on MVTec-loco [Bergmann *et al.*, 2022a].

AUC Class	Algorithm	Single class based			Multi-class based		
		PatchCore	DDAD	CCAD(V)	DiAD	CCAD(C)	CCAD(F)
breakfast box		0.609; 0.743	0.914; 0.870	0.966; 0.872	0.533; 0.772	0.560; 0.794	0.561 ; 0.751
juice bottle		0.783; 0.583	0.989; 0.833	0.997; 0.849	0.883; 0.893	0.919; 0.898	0.882; 0.893
pushpins		0.648; 0.653	0.819; 0.612	0.854 ; 0.635	0.703 ; 0.576	0.662; 0.593	0.655; 0.597
screw bag		0.596; 0.658	0.741; 0.479	0.749 ; 0.503	0.559; 0.723	0.542; 0.720	0.561 ; 0.717
splicing connectors		0.633; 0.578	0.969; 0.598	0.920; 0.591	0.650; 0.604	0.669; 0.588	0.692; 0.617
mean		0.654; 0.643	0.886; 0.678	0.897; 0.690	0.665; 0.714	0.671; 0.718	0.670; 0.715

Table 12: F1 score (Class-level; Pixel-level) on MVTec-loco with DiAD, CCAD(C & F).

Table 13: Average precision (Class-level; Pixel-level) on MVTec-loco with DiAD, CCAD(C & F).

F1	DiAD	CCAD(C)	CCAD(F)	AP	DiAD	CCAD(C)	CCAD(F)
				breakfast box	juice bottle	pushpins	screw bag
breakfast box	0.772; 0.331	0.772 ; 0.131	0.772 ; 0.314	0.728; 0.237	0.622; 0.051	0.732 ; 0.230	
juice bottle	0.888 ; 0.471	0.834; 0.222	0.881; 0.483	0.963 ; 0.451	0.705; 0.129	0.963 ; 0.476	
pushpins	0.720 ; 0.068	0.714; 0.019	0.714; 0.073	0.707 ; 0.018	0.583; 0.008	0.689; 0.019	
screw bag	0.783; 0.140	0.782; 0.102	0.785; 0.141	0.650; 0.081	0.660; 0.054	0.690 ; 0.083	
splicing connectors	0.764; 0.186	0.764; 0.145	0.768 ; 0.168	0.786 ; 0.137	0.629; 0.092	0.753; 0.105	
mean	0.785 ; 0.239	0.773; 0.124	0.784; 0.236	0.767 ; 0.185	0.640; 0.067	0.765; 0.183	

D.4 MVTec-3d Dataset

Table 14: AUROC(Class-level; Pixel-level) comparison with SOTA methods on MVTec-3d [Bergmann *et al.*, 2022b].

AUC Class	Algorithm	Single class based			Multi-class based		
		PatchCore	DDAD	CCAD(V)	DiAD	CCAD(C)	CCAD(F)
bagel		0.671; 0.439	0.878; 0.974	0.892; 0.977	0.756; 0.990	0.955 ; 0.987	0.920; 0.983
cable gland		0.682; 0.981	0.957; 0.991	0.959; 0.994	0.842 ; 0.969	0.607; 0.977	0.553; 0.944
carrot		0.669; 0.621	0.669; 0.649	0.722; 0.824	0.804; 0.982	0.674; 0.980	0.891 ; 0.936
cookie		0.662; 0.675	0.677 ; 0.955	0.671; 0.960	0.714 ; 0.937	0.631; 0.946	0.585; 0.932
dowel		0.711; 0.995	0.996; 0.994	0.999 ; 0.994	0.837; 0.987	0.891 ; 0.985	0.769; 0.939
foam		0.671; 0.719	0.918 ; 0.867	0.914; 0.891	0.533; 0.833	0.774; 0.944	0.563; 0.811
peach		0.637 ; 0.498	0.559; 0.953	0.563; 0.956	0.564; 0.982	0.543; 0.987	0.594 ; 0.969
potato		0.645 ; 0.535	0.458; 0.817	0.456; 0.793	0.777; 0.985	0.647; 0.985	0.689; 0.936
rope		0.683; 0.591	0.875; 0.986	0.887; 0.987	0.741; 0.982	0.750 ; 0.974	0.697; 0.983
tire		0.666; 0.918	0.664; 0.867	0.803; 0.980	0.524; 0.921	0.619 ; 0.942	0.569; 0.944
mean		0.67; 0.697	0.765; 0.905	0.787; 0.936	0.709 ; 0.957	0.709; 0.971	0.683; 0.938

Table 15: F1 score (Class-level; Pixel-level) on MVTec-3d with DiAD, CCAD(C & F)

F1	DiAD	CCAD(C)	CCAD(F)
bagel	0.960 ; 0.537	0.947; 0.545	0.927; 0.422
cable gland	0.952 ; 0.149	0.900; 0.313	0.952 ; 0.042
carrot	0.927; 0.308	0.894; 0.286	0.941 ; 0.079
cookie	0.902 ; 0.262	0.875; 0.165	0.902 ; 0.242
dowel	0.898; 0.324	0.957; 0.396	0.958 ; 0.065
foam	0.857; 0.349	0.919; 0.231	0.947 ; 0.114
peach	0.926 ; 0.380	0.894; 0.265	0.926 ; 0.131
potato	0.955; 0.296	0.926; 0.232	0.978 ; 0.051
rope	0.762; 0.451	0.769; 0.476	0.833 ; 0.369
tire	0.963 ; 0.104	0.818; 0.117	0.902; 0.076
mean	0.910; 0.316	0.890; 0.303	0.927 ; 0.159

Table 16: Average precision (Class-level; Pixel-level) on MVTec-3d with DiAD, CCAD(C & F)

AP	DiAD	CCAD(C)	CCAD(F)
bagel	0.976; 0.500	0.987 ; 0.517	0.964; 0.342
cable gland	0.883; 0.077	0.905; 0.196	0.941 ; 0.018
carrot	0.980 ; 0.238	0.862; 0.240	0.957; 0.037
cookie	0.843; 0.240	0.788; 0.098	0.904 ; 0.218
dowel	0.903; 0.216	0.985 ; 0.331	0.903; 0.032
foam	0.943; 0.240	0.963; 0.122	0.971 ; 0.045
peach	0.918; 0.308	0.840; 0.224	0.920 ; 0.060
potato	0.892; 0.232	0.939 ; 0.194	0.914; 0.023
rope	0.868; 0.455	0.820; 0.449	0.903 ; 0.346
tire	0.923 ; 0.046	0.733; 0.046	0.840; 0.027
mean	0.913; 0.255	0.882; 0.242	0.922 ; 0.115

Table 17: Minimal epochs required to reach the same AUC level on each dataset.

eph	DiAD	CCAD (C)	CCAD (F)	AUC Lv
MVTec-AD	200	100	110	0.958; 0.958
VisA	200	60	180	0.749; 0.901
MVTec-3d	200	75	10	0.784; 0.969
MVTec-loco	200	120	120	0.668; 0.719
MTD	190	110	180	0.956; 0.821

Table 18: AUROC(Class-level; Pixel-level) on datasets with different ξ in CCAD(C & F).

ξ	AUROC		CCAD(C)		CCAD(F)	
	10	100	10	100	10	100
MVTec-AD	0.960 ; 0.963	0.957; 0.961	0.955 ; 0.964	0.953; 0.961		
DAGM	0.825 ; 0.932	0.823; 0.932	0.812; 0.924	0.830 ; 0.933		
MVTec-3d	0.780; 0.970	0.781 ; 0.972	0.649 ; 0.942	0.636; 0.939		

Shown in table 6 - 16, we list AUROC, F1 score and AP on MVTec-AD [Bergmann *et al.*, 2019], VisA [Zou *et al.*, 2022], MVTec-loco [Bergmann *et al.*, 2022a] and MVTec-3d [Bergmann *et al.*, 2019]. Extensive experimental data has consistently demonstrated that both CCAD(C) and CCAD(F) exhibit a performance advantage over DiAD across various metrics. Furthermore, CCAD(V) demonstrates a similar performance advantage when compared to both DDAD and Patchcore. This superiority is observed in multiple aspects of the evaluation, indicating that CCAD generally achieves more robust and reliable results in comparison to DiAD, DDAD, and Patchcore.

D.5 Faster Convergence in CCAD

In table 17, CCAD(C) and CCAD(F) achieve the same AUC level faster than DiAD, which we attribute to the introduction of feature banks. These conditions contribute significantly by letting the model learn relevant and representative features of the overall dataset more efficiently, thereby accelerating the convergence process.

D.6 Ablation Studies on different ξ

We conducted a comparative analysis of the AUC performance of DiAD, CCAD(C), and CCAD(F) across different ξ settings on multiple datasets. Notably, even when the ξ value is as low as 10, the AUC remains significantly high. This indicates that only a few samples are sufficient to serve as conditions, enabling the model to efficiently reconstruct normal images. This efficiency highlights the strength of the CCAD models in leveraging minimal conditions to achieve robust image reconstruction, which is crucial for effective anomaly detection.

D.7 DAGM re-annotation comparison

Shown in figure 7, we compare the AUC performance of the original DAGM2007 dataset [Wieler *et al.*, 2007] with our re-annotated dataset on SOTAs. Under the same methods, we observed that the class-wise AUC remains similar and the pixel-wise AUC significantly improved. This indicates that our labeled data is better aligned with the anomaly detection task compared to the original data.

E Hyperparameters Setting

As shown in table 19, we provide a summary of hyperparameter for our proposed algorithms. To further validate our approach, we have included additional detailed hyperparameters below to address the results. We also listed the source code of each SOTA in table 20 and hyperparameters of each experiment in table 21 and 22 to demonstrate the validity.

Table 19: Hyper-parameter Setting.

Hyper-parameter	CCAD(V)	CCAD(C)	CCAD(F)
# of Epoch	500-3000	50-200	50-200
# of Trainable Parameters	45.3M	1.4B	1.5B
Batchsize	32	12	12
Pretrain Feature Extractor	WideResNet101	ResNet50	ResNet50
Learning Rate	3×10^{-4}	$1 \times 10^{-6} - 1 \times 10^{-4}$	$1 \times 10^{-6} - 1 \times 10^{-4}$
Model Input	$256 \times 256 \times 3$	$256 \times 256 \times 3$	$256 \times 256 \times 3$
Optimizer	Adam	AdamW	AdamW
Weight decay	0.05	0.05	0.05

Table 20: Source code link.

SOTA	link
PatchCore	https://github.com/LuigiFederico/PatchCore-for-Industrial-Anomaly-Detection/tree/main
SPADE	https://github.com/byungjae89/SPADE-pytorch
DDAD	https://github.com/arimousa/DDAD/tree/main
DiAD	https://github.com/lewandofskee/DiAD

Table 21: Abbreviations and Their Corresponding Definitions in the Experimental Setup.

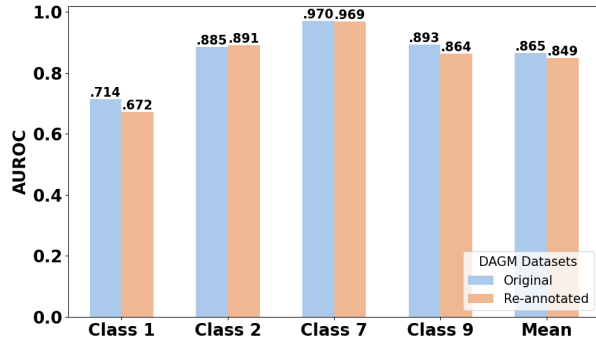
abbreviation	meaning
PFE	Pretrained feature extractor
ξ	# of samples
ℓ	learning rate
eph	# of epochs
B_s	Batch size

F Data Visualization

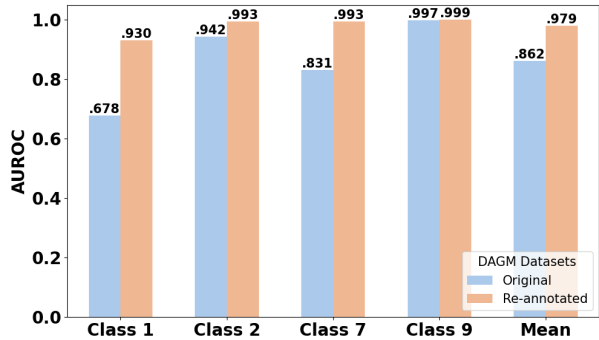
More Qualitative example visualization can be seen in figure 8 and 9.

G Acknowledge

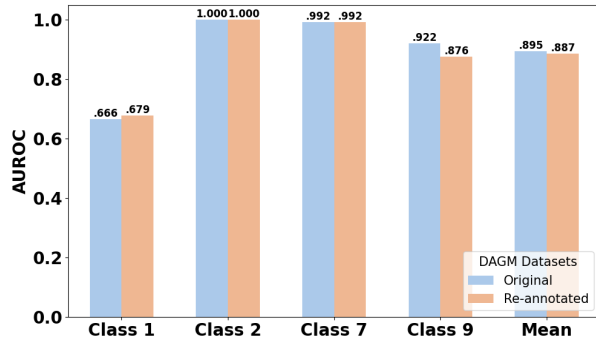
This work was supported by VisionX LLC. Models are trained on 8 NVIDIA A800 80GB PCIs and 8 NVIDIA GeForce RTX 3090s



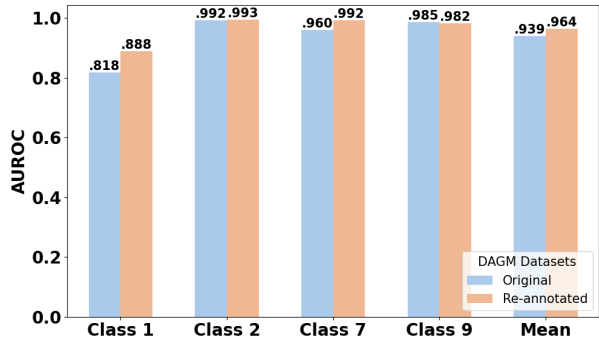
(a) Class-wise AUC on PatchCore



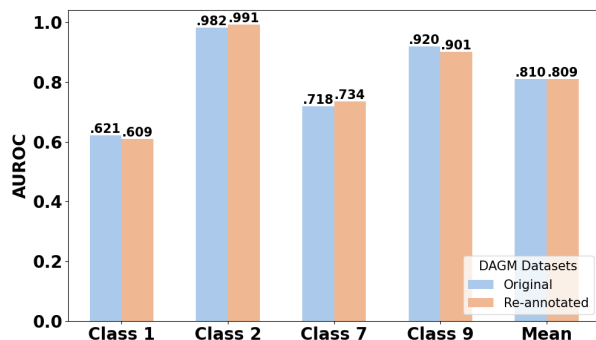
(b) Pixel-wise AUC on PatchCore



(c) Class-wise AUC on DDAD



(d) Pixel-wise AUC on DDAD



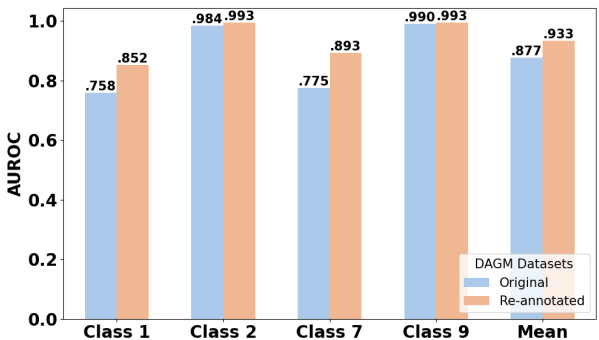
(e) Class-wise AUC on DiAD



(f) Pixel-wise AUC on DiAD



(g) Class-wise AUC on CCAD (C)

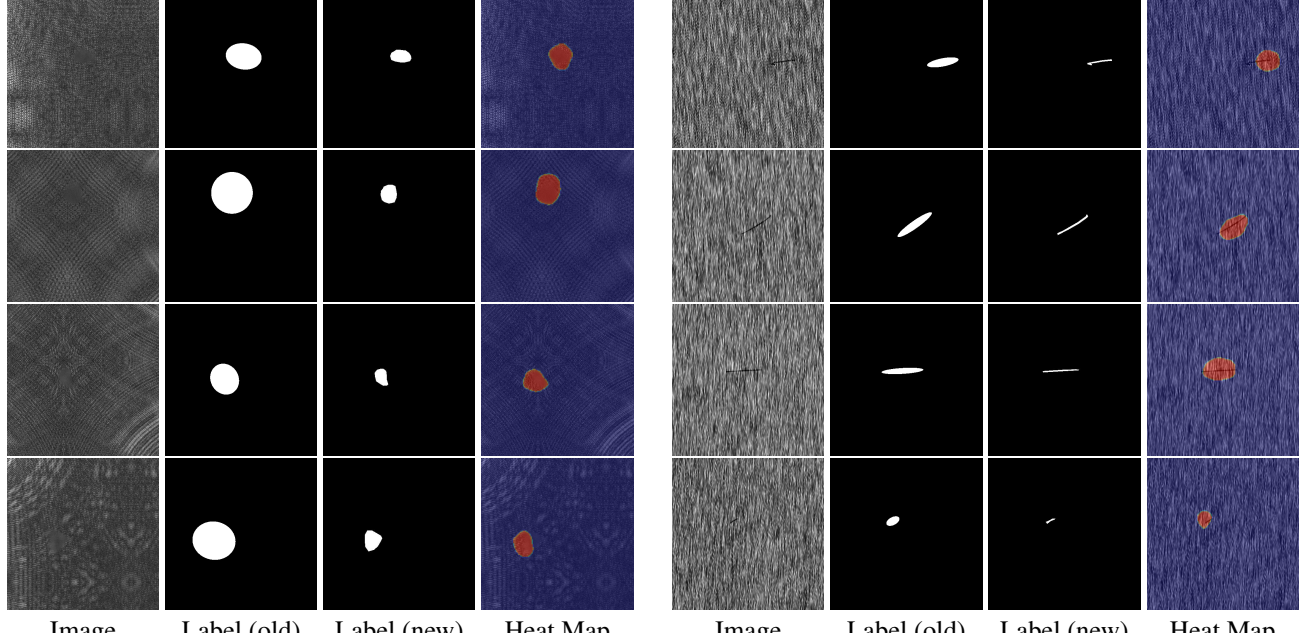


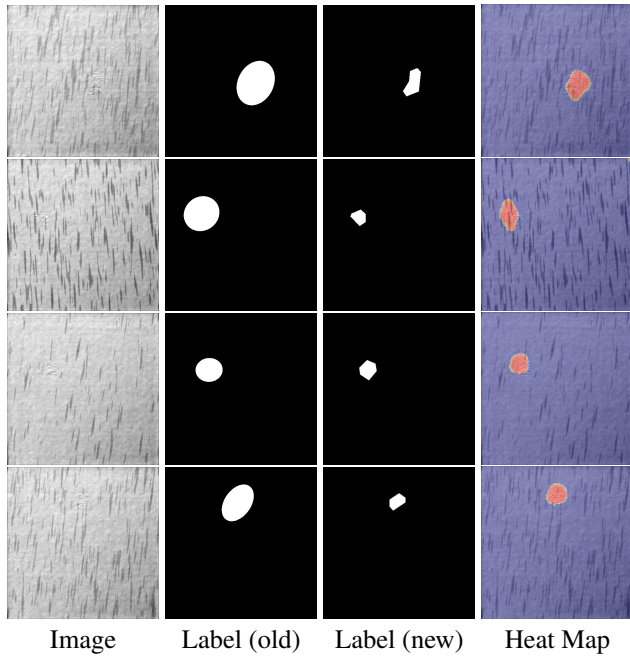
(h) Pixel-wise AUC of DAGM on STOAs

Figure 7: Class-wise AUC of DAGM on STOAs

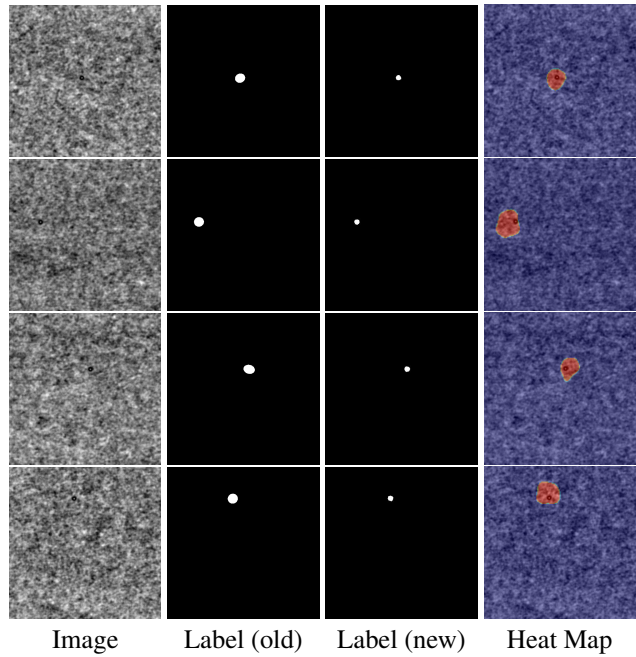
Table 22: Hyper-parameter setting of SOTA on different datasets[Esser *et al.*, 2021; He *et al.*, 2016].

Hyperparameter	Algorithm	Single class based			Multi-class based		
		PatchCore [Roth <i>et al.</i> , 2022]	DDAD [Mousakhan <i>et al.</i> , 2023]	CCAD(V)	DiAD [He <i>et al.</i> , 2024]	CCAD(C)	CCAD(F)
Hyperparameters		PFE; ξ	$eph^*; \ell$	$eph^*; \ell; \xi$	PFE; $\xi; \ell; eph; Bs$	PFE; $\xi; \ell; eph; Bs$	PFE; $\xi; \ell; eph; Bs$
MVTec-AD[Bergmann <i>et al.</i> , 2019]	AutoEncoderKL; 1000	500 – 2000; 3×10^{-4}	500 – 2000; $3 \times 10^{-4}; 200$		ResNet50; 1000; $1 \times 10^{-4}; 200; 12$	ResNet50; 1000; $1 \times 10^{-4}; 200; 12$	ResNet50; 1000; $5 \times 10^{-5}; 200; 12$
VisA[Zou <i>et al.</i> , 2022]	AutoEncoderKL; 1000	500 – 1000; 3×10^{-4}	1000; $3 \times 10^{-4}; 200$		ResNet50; 1000; $1 \times 10^{-5}; 150; 12$	ResNet50; 1000; $4.5 \times 10^{-6}; 150; 12$	ResNet50; 1000; $5 \times 10^{-6}; 150; 12$
MVTec-3d[Bergmann <i>et al.</i> , 2022b]	AutoEncoderKL; 1000	500 3×10^{-4}	500 – 1000 $3 \times 10^{-4}; 200$		ResNet50; 1000; $1 \times 10^{-4}; 100; 12$	ResNet50; 1000; $5 \times 10^{-5}; 100; 12$	ResNet50; 1000; $2 \times 10^{-5}; 100; 12$
MVTec-loco[Bergmann <i>et al.</i> , 2022a]	AutoEncoderKL; 1000	500 – 1000; 3×10^{-4}	500 – 1000; $3 \times 10^{-4}; 200$		ResNet50; 1000; $1 \times 10^{-5}; 200; 12$	ResNet50; 1000; $1 \times 10^{-5}; 200; 12$	ResNet50; 1000; $1 \times 10^{-5}; 200; 12$
MTD[Huang <i>et al.</i> , 2018]	AutoEncoderKL; 1000	1000; 3×10^{-4}	1000; $3 \times 10^{-4}; 200$		ResNet50; 1000; $1 \times 10^{-4}; 200; 12$	ResNet50; 1000; $1 \times 10^{-4}; 200; 12$	ResNet50; 1000; $5 \times 10^{-5}; 200; 12$
DAGM 2007[Wieler <i>et al.</i> , 2007]	AutoEncoderKL; 1000	1000 – 2500; 3×10^{-4}	1000 – 2500; $3 \times 10^{-4}; 200$		ResNet50; 1000; $1 \times 10^{-5}; 40; 12$	ResNet50; 1000; $1 \times 10^{-5}; 40; 12$	ResNet50; 1000; $1 \times 10^{-5}; 40; 12$
different ξ on MVTec-AD	–	500 – 2000; 3×10^{-4}	500 – 2000; $3 \times 10^{-4}; 10 \& 200$		–	–	–



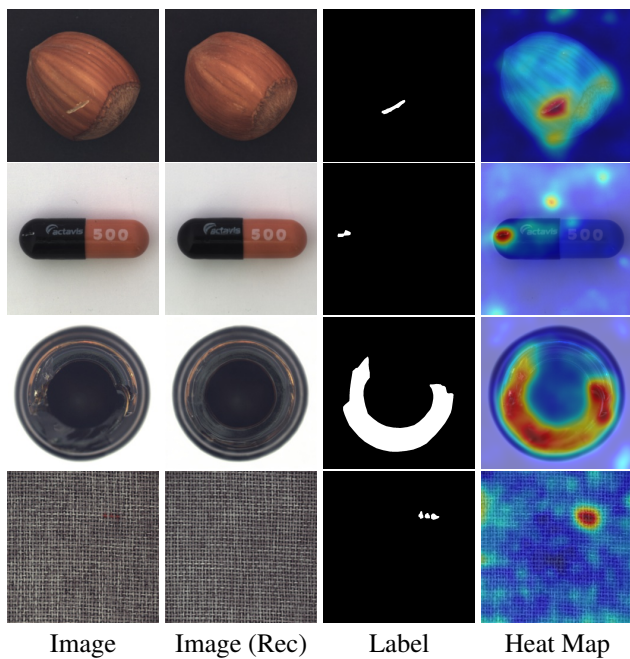


(c) Visualization of DAGM Class 7

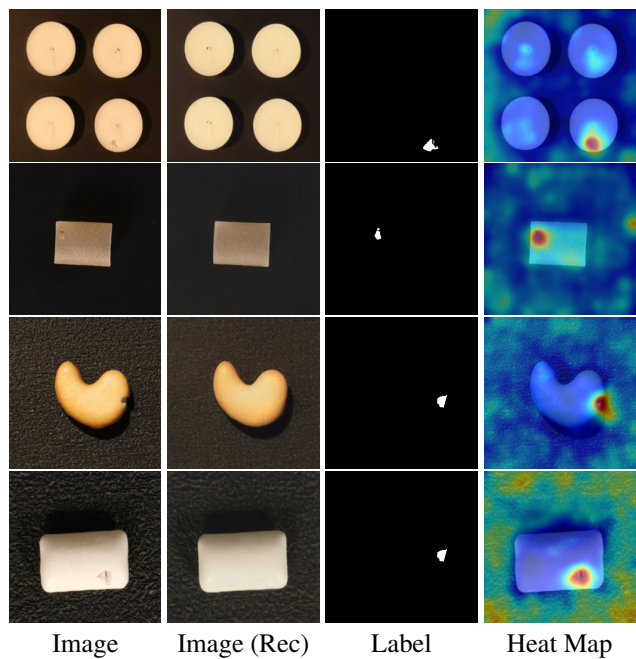


(d) Visualization of DAGM Class 2

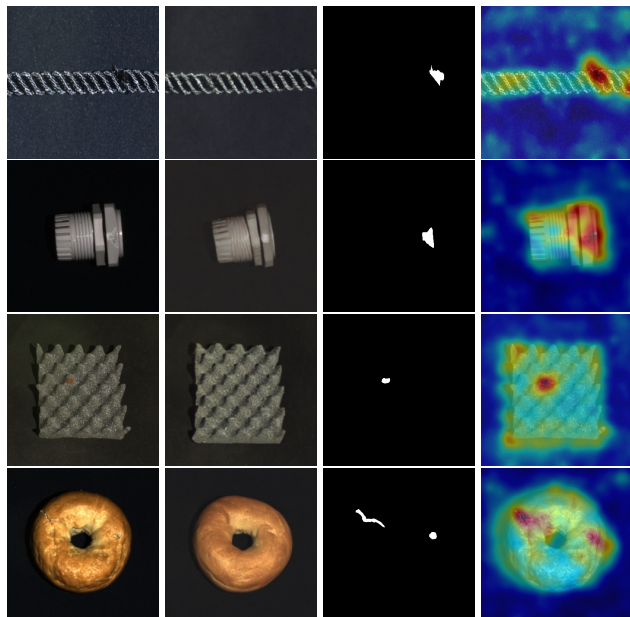
Figure 8: Qualitative example visualization on DAGM



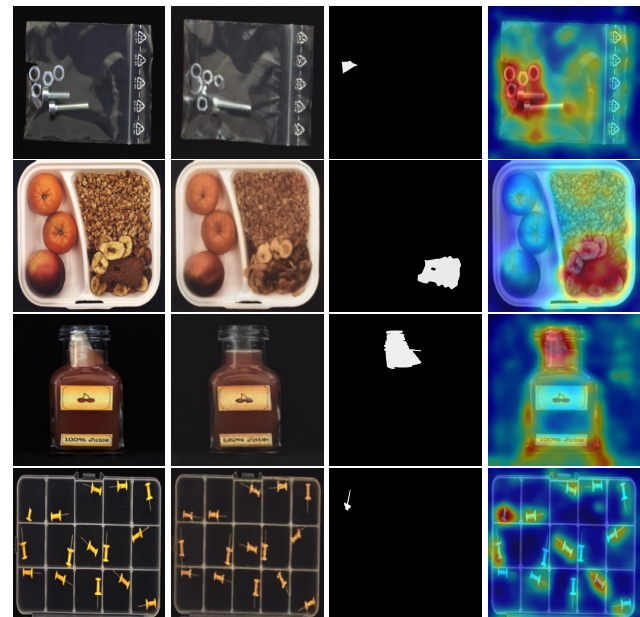
(a) Visualization of MVTec-AD [Bergmann *et al.*, 2019]



(b) Visualization of VisA [Zou *et al.*, 2022]



(c) Visualization of MVTec-3d [Bergmann *et al.*, 2022b]



(d) Visualization of MVTec-Loco [Bergmann *et al.*, 2022a]

Figure 9: Qualitative example visualization on Datasets